Mon. Not. R. Astron. Soc. **272,** 749–762 (1995)

The *Ginga* hard X-ray spectrum of AM Herculis

A. P. Beardmore,[1]★ C. Done,[1]† J. P. Osborne[1] and M. Ishida[2]

[1] *X-ray Astronomy Group, Department of Physics &Astronomy, University of Leicester, Leicester LE1 7RH*

[2] *Institutè of Space and Astronautical Science 3-1-1 Yoshinodai, Sagamihara, Kanagawa 229, Japan*

Accepted 1994 September 12. Received 1994 September 7; in original form 1994 January 5

ABSTRACT

We present an analysis of the phase-resolved 2–30 keV X-ray spectrum of the prototype magnetic cataclysmic variable AM Herculis obtained with the *Ginga* satellite. The bremsstrahlung flux varies by more than a factor of 7 as a function of orbital phase, demonstrating that the X-ray orbital intensity variation is due to partial occultation which varies with the viewing angle. The spectrum is hardest when the source is brightest in its orbital cycle, and the phase-resolved spectra are not well fitted by simple models with a narrow line plus continuum. The derived high and variable bremsstrahlung temperature cannot account for the observed line emission, and the residuals to these fits indicate complex behaviour at high and low energies. The latter is shown to be consistent with a complex absorber, and both partial covering and partial ionization give a good description of the soft spectrum. The residuals above 6 keV are well modelled by reflection from the white dwarf surface, where the amount of reflection varies with phase as predicted by the changing inclination of the white dwarf surface. The inclusion of this hard and variable spectral component gives a temperature for the post-shock region of ~13.5 keV, which is constant with phase. This value is considerably lower than previous estimates, allowing the high equivalent width of the iron line to be explained as a combination of a thermal line blend at 6.8 keV and a 6.4-keV fluorescent component. This new low bremsstrahlung temperature suggests that the hard X-ray luminosities of AM Her systems may have been overestimated, exacerbating the soft X-ray problem. The detailed modelling of the complex low-energy spectrum affects the derived ionization state of the reflector: with partial covering of cold material the reflection spectrum is significantly ionized, but with an ionized absorber the reflecting surface is cold.

Key words: binaries: close – stars: individual: AM Her – stars: magnetic fields – novae, cataclysmic variables – X-rays: stars.

1 INTRODUCTION

AM Herculis is the prototype of the magnetic cataclysmic variable class known as polars. These are binary systems in which a strongly magnetic white dwarf is synchronously locked to a red dwarf companion from which it accretes gas via Roche lobe overflow. The magnetic field of the white dwarf is sufficiently strong ($B \simeq 30$ MG) to prevent the formation of an accretion disc. Hard X-ray bremsstrahlung radiation is emitted from a hot post-shock accretion region ($T \sim$ few $\times 10^8$ K) close to the white dwarf surface. Cropper (1990) gives a comprehensive review of the class.

In spite of the fact that magnetic cataclysmic variables (CVs) are expected to have a common X-ray emission mechanism, X-ray spectral studies have not converged on a common interpretation. This has been partly due to limitations of the detectors, partly due to uncertainties in modelling the high absorption seen in the non-synchronous intermediate polars, and partly due to the fact that one of the brightest magnetic cataclysmic variables, EX Hya, appears to be atypical. The continua of other systems have been fitted by power-law or high-temperature bremsstrahlung spectra (e.g. Norton & Watson 1989). Norton, Watson & King (1991) require a continuous distribution of absorbing column densities to model the high iron line equivalent

★ Present address: Department of Physics, The Open University, Walton Hall, Milton Keynes MK7 6AA.

† Present address: Department of Physics, University of Durham, South Road, Durham DH1 3LE.

widths seen in the other intermediate polars; however, this model does not fit the line emission of EX Hya, which appears to be thermal rather than fluorescent. Ishida (1991) shows that, in general, iron line emission is not consistent with observed continuum temperatures. Observations of EX Hya at higher spectral resolution require two distinct continuum temperatures (Singh & Swank 1993); the continuous distribution of temperatures expected for the post-shock region is not seen. This model predicts an iron line energy significantly higher than that observed (Ishida et al. 1994). Singh & Swank (1993) and Kallman et al. (1993) report the presence of cool or cold X-ray spectral features in EX Hya and BY Cam, respectively. However, Kallman et al. (1993) do not see cool iron fluorescence in BY Cam, suggesting that reprocessing occurs in a hot layer on the white dwarf.

As the strongest polar X-ray source, AM Her has been observed with several X-ray satellites (Crosa et al. 1981; Rothschild et al. 1981; Tuohy et al. 1981; Heise et al. 1985). *HEAO-1* X-ray observations reported by Rothschild et al. (1981) revealed that a single bremsstrahlung temperature did not describe the hard X-ray data – the spectra were too flat at 10 keV and too steep at 30 keV. As this was suggestive of a component reflected from the white dwarf surface (Felsteiner & Opher 1976), they extended their model to two thermal bremsstrahlung continua at the same temperature, but absorbed by different column densities, to estimate an albedo of 0.1–0.3. By fitting their data above 10 keV, where energy-dependent albedo effects were not thought to be important, they obtained a temperature of 30.9 ± 4.5 keV. The *HEAO-1* data also showed strong iron–K line emission at an energy of 6.5 ± 0.15 keV and with an equivalent width of 0.8 ± 0.1 keV. As the amount of line emission was too great to be of thermal origin, Rothschild et al. (1981) proposed that fluorescence from the white dwarf surface could be responsible. The calculations of Basko (1978) and Bai (1979), however, implied that a fluorescent line equivalent width would be $\lesssim 0.3$ keV. Taking this one stage further, Swank, Fabian & Ross (1984) performed Monte Carlo calculations of the accretion column and white dwarf surface together. These included the effects of scattering and fluorescence excited by photons created from a 30-keV thermal continuum. Their results showed that the observed continuum shape and line equivalent width could be produced from an accretion column of cross-sectional optical depth 0.2–0.7, but only if an additional thermal component of 2–10 keV was present.

Recent improvements in the description of reflection (Lightman & White 1988; George & Fabian 1991; Matt, Perola & Piro 1991) have been applied to recent *Ginga* X-ray spectra of active galactic nuclei (Pounds et al. 1990), black hole candidates (Done et al. 1992), and X-ray binaries (Yoshida et al. 1993), where the X-rays are thought to illuminate the accretion disc. In magnetic CVs, however, the white dwarf surface subtends a solid angle of $\sim 2\pi$ with respect to the optically thin emission region, and we expect to see reflection in such systems.

In this paper, we present *Ginga* hard X-ray observations of AM Her. We show that the spectrum can most simply be modelled by an isothermal continuum plus a reflected component from the white dwarf surface. The presence of reflection allows the temperature of the thermal component to be reduced with respect to a simple thermal fit. This, together with the fluorescence caused by reflection, provides an explanation for the observed iron line equivalent width.

2 OBSERVATIONS AND ANALYSIS

AM Her was observed with the LAC of *Ginga* from 1989 September 17 at 20:03 (UT) to 1989 September 21 at 12:18 (UT). As *Ginga* has no provision for a simultaneous background measurement, one day in-between was devoted to an observation of a nearby off-source region (see Table 1), so that a suitable model of the X-ray background could be made. Both observations were taken in MPC-1 mode, which covers the energy range 1.2–37.0 keV in 48 pulse height channels (Turner et al. 1989), and analysis was restricted to using count rates recorded in the top layer of the LAC.

The background was estimated using a variation of the method described by Hayashida et al. (1989). This involves characterizing the off-source count rate in terms of geomagnetic and auxiliary parameters, and using these to reconstruct the background at the time of the source observation. After completion of the background subtraction, the data were checked for anomalies. It was found that, from 00:30 to 09:30 UT on September 19, intense flaring was seen in the lower PHA channels, separated precisely by the *Ginga* orbital period of 95 min. Although nothing anomalous was detected in the *Ginga* housekeeping parameters, plots of planetary K indices and magnetometer data (Kellet, private communication) revealed that an intense geomagnetic storm occurred at this time. It appears that *Ginga* passed through a region of enhanced particle flux in the upper atmosphere, located between longitudes $-110°$ to $150°$ and latitudes $+10°$ to $+30°$, for six consecutive orbits, causing data contamination. In subsequent analyses, the data from this period were excluded, leaving a total exposure of 74 400 s.

Fig. 1(a) shows the 1.7–18.0 keV light curve for the latter part of the observation at 128-s binning. The hard X-ray light curve is similar to that seen in previous observations (Crosa et al. 1981; Heise et al. 1985), showing a minimum at linear polarization phase 0.12 (using the ephemeris of Wickramasinghe et al. 1991) and a maximum half a cycle later. The maxima are dominated by flickering on a time-scale ranging from several tens to several hundred seconds. Studies of this variability will be presented elsewhere. The flux at maximum was 2.25×10^{-10} erg cm^{-2} s^{-1} (in the 2–30 keV band), consistent with the *HEAO-1* observations of Rothschild et al. (1981), but a factor of 6 brighter than the *EXOSAT* observations reported by Heise et al. (1985), when AM Her was in the anomalous state. Photometry obtained at the Nordic Optical Telescope on 1989 September 20 at 20:45 (UT), for one binary period, revealed a mean *V*-band magnitude of 13.7, indicating that AM Her was in an intermediate-brightness state.

Table 1. *Ginga* observation log for AM Her and a nearby background.

Source	RA° (1950)	DEC° (1950)	Start (UT)	Stop (UT)
AM Her	273.74	+49.85	17-Sep-1989 20:03	19-Sep-1989 18:00
Background	272.30	+47.50	19-Sep-1989 18:00	20-Sep-1989 18:02
AM Her	273.74	+49.85	20-Sep-1989 18:02	21-Sep-1989 12:18

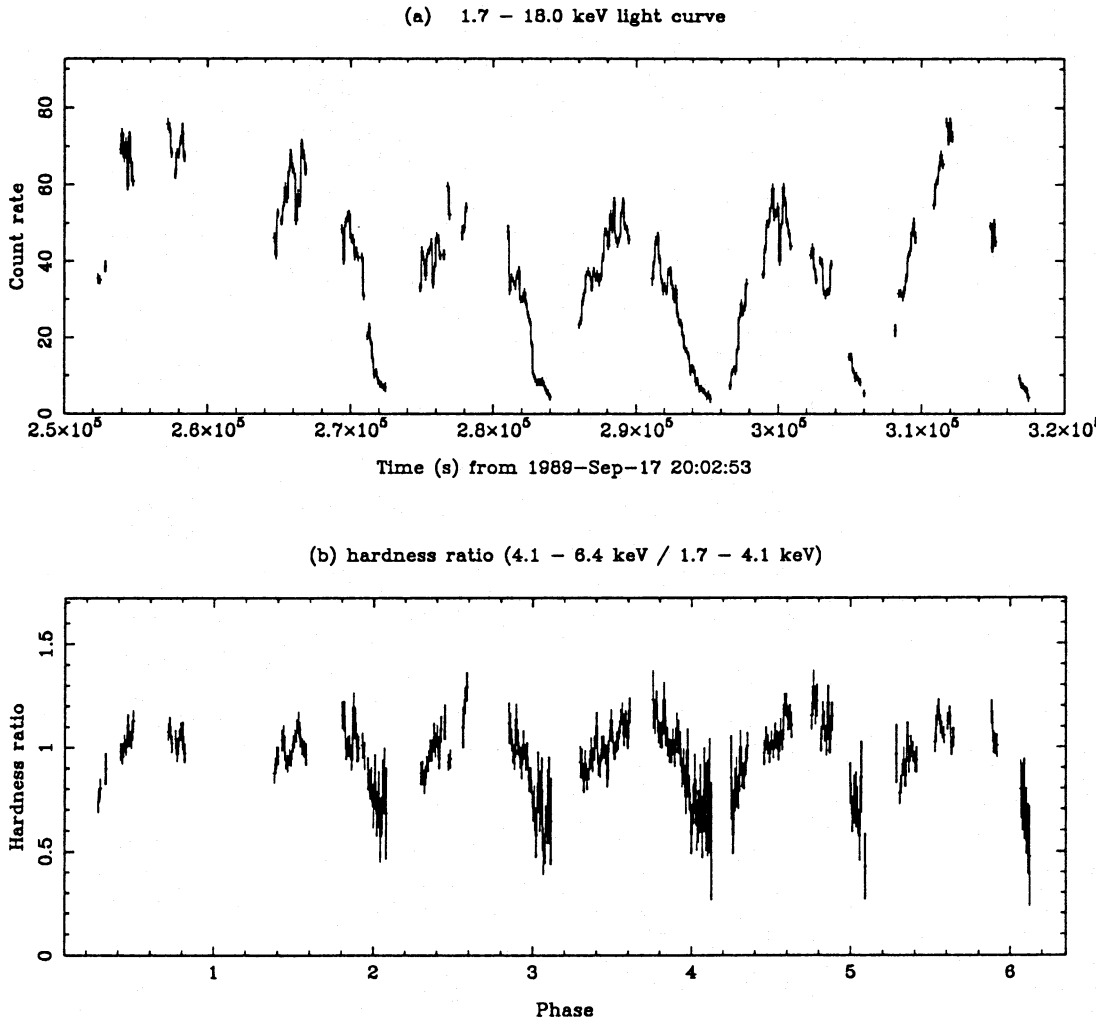

Figure 1. (a) Part of the background-subtracted 1.7–18.0 keV *Ginga* light curve of AM Her. (b) Hardness ratio (4.1–6.4 keV/1.7–4.1 keV) showing a clear spectral variation through the orbital cycle.

The hardness ratio, 4.1–6.4 keV/1.7–4.1 keV, is plotted in Fig. 1(b). This shows a clear spectral variation through the orbital cycle, with the source becoming harder when brighter. Because of this, any interpretation of a phase-averaged spectrum will not be correct, so we describe only results obtained from phase-resolved spectral fitting.

3 SPECTRAL MODEL FITS

3.1 Thermal bremsstrahlung, narrow line and absorption

The data were folded into 10 phase bins, using the linear polarization ephemeris of Wickramasinghe et al. (1991). The first model fitting to the data was a thermal bremsstrahlung continuum, at temperature $kT_{\rm br}$, plus narrow line, with absorption at low energy due to a uniform column, $N_{\rm H}$, of cold gas (i.e. five free parameters). Cross-sections and abundances were taken from Morrison & McCammon (1983). Systematic errors of 1 per cent were included in the data. The parameters and reduced χ^2 obtained to the fits are summarized in Table 2. Only in phase bins 1 to 3 (phase $\phi = 0.0$–0.3), when the intensity is low, is there acceptable agreement between this model and the data (reduced $\chi^2 < 1.22$). This simple model becomes inadequate as the source brightens, with residuals at low energies indicating a complex absorption behaviour, and a strong deviation around 6–9 keV (see Fig. 2a).

This model is also difficult to explain theoretically, as the temperature varies strongly with phase, with $kT_{\rm br}$ ranging from 9 to 36 keV. Such variation is not expected if the changes in the spectrum are caused by occultation of an optically thin region by the white dwarf surface. Also, the line equivalent width, which varies from 0.43 ± 0.08 keV at phase 0.25 to 0.76 ± 0.04 keV at phase 0.55, is far too large to be produced from a solar abundance plasma at the temperatures inferred, and the line energy (6.67 ± 0.03 keV) is rather lower than predicted (Raymond & Smith 1977).

3.2 Thermal bremsstrahlung, narrow line, and a partial-covering absorber

Spatial non-uniformity in the absorbing medium (i.e. partial covering) can cause absorption of medium-energy X-rays

Table 2. Results of absorbed thermal bremsstrahlung plus narrow-line fits to the phase-resolved data of AM Her. Errors are 68 per cent, $\Delta\chi^2 = 2.30$, confidence estimates.

Phase bin (phase range)	$N_{br}{}^a$ ($\times 10^{-3}$)	$kT_{br}{}^b$	$E_l{}^c$	W^d	$N_H{}^e$	χ^2_ν (29 d.o.f.)
1 (0.0–0.1)	$1.9^{+0.2}_{-0.2}$	$11.3^{+1.6}_{-1.1}$	$6.74^{+0.15}_{-0.18}$	$0.55^{+0.13}_{-0.14}$	< 1.2	0.86
2 (0.1–0.2)	$1.3^{+0.3}_{-0.2}$	$9.3^{+1.9}_{-0.4}$	$6.71^{+0.21}_{-0.18}$	$0.71^{+0.29}_{-0.26}$	< 1.7	1.22
3 (0.2–0.3)	$3.2^{+0.3}_{-0.2}$	$15.4^{+1.5}_{-1.7}$	$6.67^{+0.17}_{-0.12}$	$0.43^{+0.08}_{-0.08}$	< 1.8	0.70
4 (0.3–0.4)	$5.3^{+0.2}_{-0.2}$	$25.5^{+1.6}_{-1.4}$	$6.67^{+0.05}_{-0.04}$	$0.49^{+0.03}_{-0.04}$	$5.2^{+1.0}_{-0.8}$	2.35
5 (0.4–0.5)	$6.4^{+0.2}_{-0.2}$	$28.1^{+1.6}_{-1.5}$	$6.65^{+0.03}_{-0.03}$	$0.65^{+0.03}_{-0.03}$	$8.3^{+0.8}_{-0.8}$	4.47
6 (0.5–0.6)	$6.3^{+0.3}_{-0.3}$	$36.4^{+3.1}_{-2.5}$	$6.66^{+0.03}_{-0.03}$	$0.76^{+0.04}_{-0.04}$	$11.1^{+0.9}_{-1.0}$	4.57
7 (0.6–0.7)	$6.7^{+0.3}_{-0.3}$	$33.3^{+3.0}_{-2.5}$	$6.66^{+0.03}_{-0.03}$	$0.75^{+0.04}_{-0.04}$	$13.7^{+1.1}_{-1.1}$	3.24
8 (0.7–0.8)	$7.1^{+0.5}_{-0.3}$	$29.1^{+2.3}_{-2.5}$	$6.66^{+0.03}_{-0.03}$	$0.73^{+0.04}_{-0.04}$	$15.5^{+1.0}_{-1.1}$	4.62
9 (0.8–0.9)	$5.9^{+0.2}_{-0.2}$	$29.1^{+2.2}_{-1.8}$	$6.62^{+0.04}_{-0.03}$	$0.59^{+0.03}_{-0.03}$	$12.1^{+0.9}_{-1.0}$	2.66
10 (0.9–1.0)	$4.3^{+0.2}_{-0.2}$	$23.3^{+1.7}_{-1.5}$	$6.77^{+0.05}_{-0.05}$	$0.47^{+0.04}_{-0.04}$	$6.5^{+1.0}_{-1.0}$	1.85

[a]Bremsstrahlung normalization $= 3.0 \times 10^{-15} kT_{br}^{-1/2} S/(4\pi d^2)$, where S = emission measure (cm^{-3}), d = distance (cm); [b]bremsstrahlung temperature (keV); [c]line energy (keV); [d]line equivalent width (keV); [e]column density (10^{21} cm^{-2}).

while still allowing lower energy X-rays to escape. Given the residuals to the previous model, the partial-covering model offered the possibility of a better fit. The model for phase bins 4–10 was extended to include partial covering by assuming that the absorbing column, N_H, covered a fraction C_F of the continuum source (six free parameters). The fitting parameters are shown in Table 3. The reduced χ^2 improved substantially for each phase bin, although it only became truly acceptable for phase bin 10. As the residuals to these fits show (Fig. 2b), the partial-covering model fits the continuum well below 6 keV. The line energy was constant at 6.71 ± 0.02 keV [$\chi^2_\nu = 0.64$ for 6 degrees of freedom (dof) against a constant hypothesis], in agreement with the value obtained for phase bins 1–3 above. The line equivalent width again varied with the source intensity, peaking at 0.62 ± 0.05 keV in phase bin 7 ($\phi = 0.6$–0.7). Absorbing column densities of 1×10^{23} cm^{-2} were required, with the covered fraction changing from 30 to 50 per cent as the source brightened. The bremsstrahlung emission is now consistent with a constant temperature for phase bins 4–10, with $kT_{br} = 19.4$ keV ($\chi^2_\nu = 0.5$, 6 dof), although this is significantly higher than in phase bins 1–3 for the simpler model above. For an optically thin plasma at this temperature, however, we would expect a line at an energy of 6.9 keV, with an equivalent width of no more than 0.2 keV (Raymond & Smith 1977), in clear contradiction to what is observed.

3.3 Thermal bremsstrahlung, broad line and a partial-covering absorber

The combination of a fluorescence line from cold iron at 6.4 keV and the thermal line from the emission region would be inextricably blended in the low-energy resolution of *Ginga* (1.08-keV FWHM at 6 keV). This might explain the anomalous line energy obtained from the previous fit, and, if there was a substantial contribution from a cold line external to the emission region, it might also reduce the problem with the large line equivalent width. The partially covered thermal bremsstrahlung plus line model fitted to phase bins 4–10 was therefore extended to include the Gaussian width of the line, σ_l, as a further free parameter (see Table 4).

Again, kT_{br}, E_l, C_F and N_H were consistent with the results obtained from a narrow line, with $kT_{br} = 21.4 \pm 1.4$ keV, $E_l = 6.71 \pm 0.03$ keV, $N_H = 8 \times 10^{22}$ cm^{-2} and C_F varying from 25 to 50 per cent. The equivalent widths obtained for the broad line fits were slightly higher than the narrow-line estimates, peaking at 0.75 ± 0.10 keV in phase bin 6 ($\phi = 0.50$–0.60). σ_l was, on average, 0.39 keV. This model gives an acceptable fit to all the data, but the mean line energy of 6.7 keV implies roughly equal amounts of line emission at 6.4 and 6.9 keV. This is much larger than the amount of line emission at 6.4 keV that can possibly be obtained from the absorbing material in the line of sight (<100 eV; Makishima 1986), and larger than could be produced from fluorescence from the white dwarf surface. Thus, although this model is statistically acceptable, it does not provide a self-consistent physical description of the data.

3.4 Thermal bremsstrahlung, narrow line, edge, and a partial-covering absorber

Above an energy of 7 keV, the main contributions to χ^2 in the narrow-line fits are due to a dip in the residuals between 8 and 10 keV, possibly indicative of an iron-K absorption edge rather than the broad line used above. A K absorption edge was therefore added to the model and, as the edge energy is a function of the ionization state of the absorbing medium (Makishima 1986), fits were tried with an edge fixed at 7.11 keV (cold iron) and 8.85 keV (He-like iron). The edge column density, N_{HFe}, defined as the iron column density divided by the cosmic abundance of iron (thus representing an equivalent hydrogen column density), was a further free parameter.

Table 5 lists the values of N_{HFe}, as well as the reduced χ^2 for the particular edge modelled. No evidence for cold iron was found, as only upper limits to N_{HFe} for a 7.11-keV edge

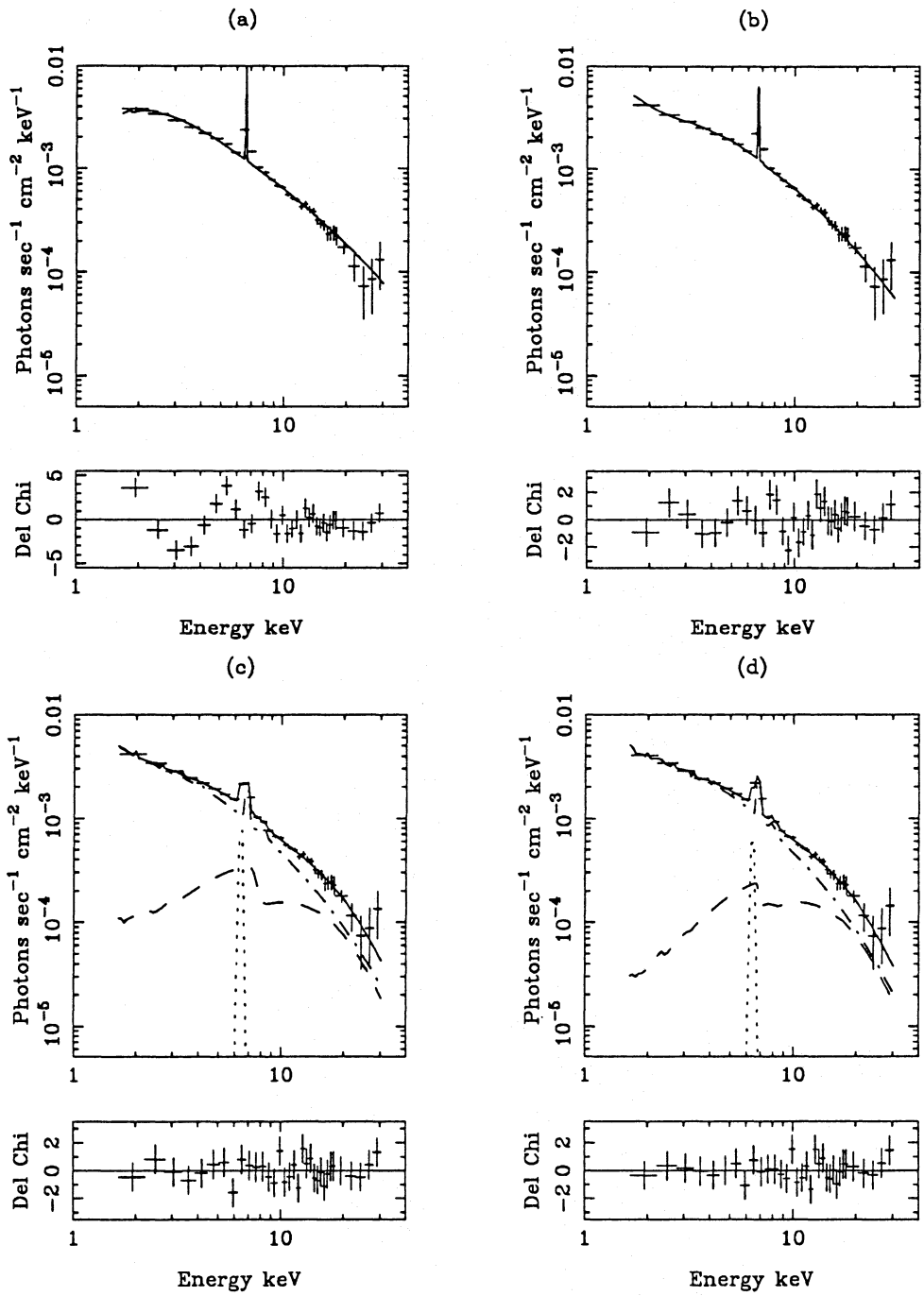

Figure 2. Sample incident spectra and residuals for phase bin 7 (phase $\phi = 0.6$–0.7) for various models discussed in the text: (a) simple thermal bremsstrahlung, iron line and absorption; (b) thermal bremsstrahlung, plus iron line, with a partial-covering absorber; (c) thermal bremsstrahlung, reflection and a partial-covering absorber; (d) thermal bremsstrahlung, reflection and an ionized absorber. Note the different residuals scale for (a).

were obtained, and there were no improvements in χ^2_ν (cf. Table 3). On the other hand, the 8.85-keV iron edge provided substantial improvements to all fits, with an average $N_{\rm HFe} = 0.9 \times 10^{23}$ cm^{-2}. The other parameters, $N_{\rm br}$, $kT_{\rm br}$, $E_{\rm l}$, W, $C_{\rm F}$ and $N_{\rm H}$, were found to be consistent with those from the model with partial covering and narrow line only. The 8.85-keV edge, along with the line energy of 6.7 keV, suggests that iron is in the high-ionization state, $\rm Fe_{XXV}$ (Makishima 1986), but once again the ionized column inferred is insufficient to produce the large equivalent width observed.

3.5 Thermal bremsstrahlung, reflection and a partial-covering absorber

As discussed earlier, the decrement in the residuals around 9 keV and the corresponding hump above 10 keV are signatures of the effects of reflection. The semi-analytic, angle-averaged, reflection model of Lightman & White (1988), including ionization effects, was used with a bremsstrahlung continuum as the illuminating flux. The ionization state of the reprocessing material was found by balancing photo-

Table 3. Fitting parameters obtained to phase bins 4–10 for the partially covered thermal bremsstrahlung and narrow iron line model. Errors are 68 per cent, $\Delta\chi^2 = 3.53$, confidence estimates.

Phase bin (phase range)	N_{br} ($\times 10^{-3}$)	kT_{br} (keV)	E_l (keV)	W (keV)	N_H (10^{23} cm^{-2})	C_F	χ^2_ν (28 d.o.f.)
4 (0.3–0.4)	$7.2^{+0.9}_{-0.9}$	$18.2^{+2.6}_{-2.1}$	$6.74^{+0.06}_{-0.08}$	$0.40^{+0.04}_{-0.04}$	$1.2^{+0.4}_{-0.4}$	$0.30^{+0.05}_{-0.05}$	1.22
5 (0.4–0.5)	$9.2^{+1.0}_{-0.9}$	$18.9^{+2.1}_{-1.7}$	$6.68^{+0.07}_{-0.04}$	$0.53^{+0.04}_{-0.04}$	$1.2^{+0.3}_{-0.3}$	$0.39^{+0.03}_{-0.03}$	1.77
6 (0.5–0.6)	$9.7^{+1.1}_{-1.0}$	$21.2^{+2.8}_{-2.3}$	$6.73^{+0.04}_{-0.06}$	$0.61^{+0.04}_{-0.04}$	$1.2^{+0.2}_{-0.2}$	$0.46^{+0.03}_{-0.03}$	1.27
7 (0.6–0.7)	$9.5^{+1.1}_{-0.8}$	$21.5^{+3.2}_{-2.6}$	$6.69^{+0.06}_{-0.05}$	$0.62^{+0.05}_{-0.05}$	$0.9^{+0.2}_{-0.2}$	$0.50^{+0.03}_{-0.03}$	1.18
8 (0.7–0.8)	$10.4^{+0.9}_{-1.1}$	$19.0^{+2.4}_{-1.7}$	$6.72^{+0.05}_{-0.06}$	$0.59^{+0.04}_{-0.04}$	$0.9^{+0.2}_{-0.2}$	$0.54^{+0.02}_{-0.02}$	1.50
9 (0.8–0.9)	$7.6^{+0.8}_{-0.7}$	$21.6^{+2.6}_{-2.3}$	$6.65^{+0.05}_{-0.05}$	$0.50^{+0.04}_{-0.04}$	$0.7^{+0.2}_{-0.2}$	$0.46^{+0.03}_{-0.03}$	1.28
10 (0.9–1.0)	$5.9^{+0.9}_{-0.8}$	$16.7^{+2.5}_{-2.1}$	$6.81^{+0.08}_{-0.07}$	$0.38^{+0.05}_{-0.05}$	$1.2^{+0.4}_{-0.4}$	$0.33^{+0.05}_{-0.05}$	0.73

Table 4. Fitting parameters obtained to phase bins 4–10 for the partially covered thermal bremsstrahlung and broad-line model. Errors are 68 per cent, $\Delta\chi^2 = 3.53$, confidence estimates.

Phase bin (phase range)	σ_l (keV)	W (keV)	χ^2_ν (27 d.o.f.)
4 (0.3–0.4)	$0.38^{+0.17}_{-0.21}$	$0.50^{+0.10}_{-0.09}$	1.02
5 (0.4–0.5)	$0.44^{+0.12}_{-0.13}$	$0.71^{+0.09}_{-0.09}$	0.95
6 (0.5–0.6)	$0.36^{+0.11}_{-0.13}$	$0.75^{+0.09}_{-0.10}$	0.80
7 (0.6–0.7)	$0.34^{+0.13}_{-0.16}$	$0.74^{+0.10}_{-0.09}$	0.89
8 (0.7–0.8)	$0.35^{+0.12}_{-0.14}$	$0.72^{+0.08}_{-0.09}$	1.12
9 (0.8–0.9)	$0.43^{+0.14}_{-0.15}$	$0.64^{+0.10}_{-0.09}$	0.81
10 (0.9–1.0)	$0.42^{+0.21}_{-0.24}$	$0.49^{+0.12}_{-0.10}$	0.52

ionizations with collisional and dielectronic recombinations to get the equilibrium populations as described in Done et al. (1992). This is characterized by the ionization parameter $\xi = L/N_e R^2$ (where L is the luminosity of the X-ray source, integrated between 5 eV and 300 keV, N_e is the number density of electrons, and R is the distance between the X-ray source and the white dwarf surface) and the temperature of the reprocessing material ($T \sim 10^5$ K). Reflection spectra were calculated for various bremsstrahlung temperatures and ionization states, and inserted into a table model for spectral fitting in XSPEC (Shafer et al. 1991). In order to include the intrinsic line emission of the X-ray-emitting gas, the thermal bremsstrahlung continuum was replaced by a Raymond & Smith model (Raymond & Smith 1977), which accounts for the correct amount of optically thin thermal line emission at a given continuum temperature. The fluorescent Kα line expected from the reflected component was fixed at 6.4 keV, with the normalization determined from spectral fitting. The equivalent width of this line then had to be checked for consistency (see below).

The above model was tried on the bright phase bins 6 and 7 ($\phi = 0.55$ and 0.65). It was found that partial covering (applied to both the incident and reflected continua) was still required to fit the data below 6 keV. The seven free parameters in the fits were, therefore, kT_{br}, N_{br}, ξ_{refl}, the reflected normalization N_{refl}, the 6.4-keV line normalization, N_H and C_F. This model was very successful, with $kT_{br} = 12.3^{+3.0}_{-2.3}$ keV, $N_{br} = 6.8^{+1.7}_{-1.5} \times 10^{-3}$, $\xi_{refl} = 110^{+220}_{-70}$, $N_{refl} = 2.0^{+1.9}_{-1.2} \times 10^{-3}$, $W_{6.4\,keV} = 0.13 \pm 0.07$ keV, $N_H = 7.4^{+2.5}_{-2.7} \times 10^{22}$ cm^{-2}, $C_F = 0.42^{+0.06}_{-0.05}$ (errors were estimated at the 68 per cent confidence level for five parameters of interest, and averaged over both phase bins), and $\chi^2_\nu = 0.63$ and 0.65 (27 dof) for phase bins 6 and 7, respectively. The thermal component, now with a temperature as low as 10 keV, can provide a line equivalent width up to 0.54 keV. This, together with the fluorescent line emission from reflection (equivalent width 0.13 keV), gives a total amount of line emission that is consistent with that observed for the non-reflection fits described earlier.

There is no reason to assume that the temperature of the emission region or the ionization state of the reprocessing material should vary as a function of phase. Therefore a simultaneous multiple-phase-bin fit was performed using the above model on the spectra from each phase bin, to test for constancy in kT_{br} and ξ_{refl}. The parameters kT_{br} and ξ_{refl} were constrained to be the same in each bin, while the remaining parameters were allowed to vary independently, resulting in 340 data points fitted with a total of 52 variable parameters. This showed that the temperature and ξ could indeed be considered constant for all phase bins, with $kT_{br} = 13.5 \pm 3.8$ keV and $\xi_{refl} = 140^{+320}_{-140}$ with $\chi^2_\nu = 0.93$ for 288 dof (errors were estimated at the 68 per cent level for 43 parameters of interest). In order to calculate uncertainties on the remaining parameters, and to reduce the computing time of these calculations, the best-fitting values of kT_{br} and ξ_{refl} were then used in fits to the 10 individual phase bins. Table 6 lists the results. Fig. 2(c) shows an example of the incident and reflected spectra obtained for phase bin 7.

As the results show, neither reflection nor partial covering was required for phase bins 1–3 ($\phi = 0.05$–0.25) when the source flux was low. For the remaining phase bins ($\phi = 0.35$–0.95), N_{br}, N_{refl} and $W_{6.4\,keV}$ increased with the source count rate, while N_H and C_F behaved as in the non-reflection fits.

3.6 Thermal bremsstrahlung, reflection and an ionized absorber

A partial-covering model behaves in the same way as a warm absorber model (e.g. Yaqoob 1991), in that both transmit low-energy X-rays (<5 keV) while absorbing medium-

Table 5. Iron edge fits to phase bins 4–10. Errors are 68 per cent, $\Delta\chi^2 = 3.53$, confidence estimates.

Phase bin (phase range)	Edge energy (keV)	N_{HFe} (10^{23} cm^{-2})	χ^2_ν (28 d.o.f.)	Edge energy (keV)	N_{HFe} (10^{23} cm^{-2})	χ^2_ν (28 d.o.f.)
4 (0.3–0.4)	7.11	< 0.2	1.25	8.85	$0.7^{+0.6}_{-0.6}$	1.09
5 (0.4–0.5)	7.11	< 0.2	1.79	8.85	$1.2^{+0.5}_{-0.5}$	1.05
6 (0.5–0.6)	7.11	< 0.3	1.29	8.85	$1.1^{+0.6}_{-0.5}$	0.80
7 (0.6–0.7)	7.11	< 0.4	1.18	8.85	$1.1^{+0.6}_{-0.6}$	0.82
8 (0.7–0.8)	7.11	< 0.2	1.51	8.85	$0.9^{+0.5}_{-0.5}$	1.15
9 (0.8–0.9)	7.11	< 0.3	1.41	8.85	$0.6^{+0.6}_{-0.5}$	1.28
10 (0.9–1.0)	7.11	< 0.1	0.96	8.85	$0.9^{+0.7}_{-0.7}$	0.78

Table 6. Summary of the parameters obtained for the partially covered reflection fits to all phase bins. kT_{br} and ξ were fixed at 13.5 keV and 140, respectively (see text). Errors are 68 per cent, $\Delta\chi^2 = 4.72$, confidence estimates.

Phase bin (phase range)	N_{br}[a] ($\times 10^{-3}$)	N_{refl}[b] ($\times 10^{-3}$)	N_{refl}/N_{br}	$W^c_{6.4}$ (keV)	N_H (10^{22} cm^{-2})	C_F	χ^2_ν (29 d.o.f.)
1 (0.0–0.1)	$1.26^{+0.05}_{-0.05}$	< 0.8	0.32 ± 0.32	$0.04^{+0.12}_{-0.04}$	< 0.12	–	0.96
2 (0.1–0.2)	$0.80^{+0.10}_{-0.10}$	< 0.7	0.41 ± 0.41	$0.04^{+0.21}_{-0.04}$	< 0.18	–	1.35
3 (0.2–0.3)	$2.25^{+0.06}_{-0.06}$	< 0.8	0.18 ± 0.18	$0.09^{+0.09}_{-0.09}$	< 0.17	–	0.72
4 (0.3–0.4)	$4.78^{+0.44}_{-0.39}$	$6.4^{+2.2}_{-2.2}$	1.32 ± 0.47	$0.05^{+0.04}_{-0.04}$	$7.4^{+5.1}_{-5.0}$	$0.23^{+0.05}_{-0.06}$	1.17
5 (0.4–0.5)	$6.09^{+0.44}_{-0.44}$	$9.7^{+2.2}_{-2.2}$	1.60 ± 0.38	$0.15^{+0.04}_{-0.04}$	$7.7^{+3.1}_{-3.1}$	$0.32^{+0.04}_{-0.04}$	0.57
6 (0.5–0.6)	$6.76^{+0.62}_{-0.59}$	$13.7^{+3.0}_{-2.9}$	2.03 ± 0.48	$0.17^{+0.04}_{-0.04}$	$8.8^{+2.8}_{-2.9}$	$0.40^{+0.04}_{-0.04}$	0.64
7 (0.6–0.7)	$6.76^{+0.65}_{-0.64}$	$13.4^{+3.4}_{-3.0}$	2.00 ± 0.50	$0.18^{+0.04}_{-0.04}$	$6.7^{+2.6}_{-2.6}$	$0.46^{+0.05}_{-0.05}$	0.65
8 (0.7–0.8)	$7.07^{+0.53}_{-0.53}$	$10.6^{+2.9}_{-2.8}$	1.51 ± 0.41	$0.18^{+0.04}_{-0.04}$	$6.9^{+2.0}_{-2.0}$	$0.51^{+0.04}_{-0.04}$	0.89
9 (0.8–0.9)	$5.45^{+0.45}_{-0.40}$	$10.4^{+2.4}_{-2.3}$	1.89 ± 0.45	$0.12^{+0.04}_{-0.04}$	$4.7^{+2.7}_{-2.4}$	$0.45^{+0.16}_{-0.05}$	0.89
10 (0.9–1.0)	$3.87^{+0.40}_{-0.35}$	$3.7^{+2.0}_{-2.1}$	0.95 ± 0.53	$0.03^{+0.07}_{-0.03}$	$7.6^{+4.8}_{-4.7}$	$0.28^{+0.05}_{-0.06}$	0.60

[a]Bremsstrahlung normalization; [b]reflected normalization; [c]6.4-keV line equivalent width.

energy X-rays. In the case of a warm absorber, photoionization strips the light elements of their K-shell electrons (those that provide the absorption in the X-ray band), which can then provide a leakage of low-energy X-rays. A warm absorber model was constructed, where the ionic populations are determined as for the ionized reflector (Done et al. 1992), and used to derive the opacity of the material directly in calculating the transmitted flux.

Spectral fitting as described for the partially covered reflection model above was repeated, this time with the absorption ionization parameter ξ_{abs} replacing the covered fraction, C_F. A simultaneous fit to the 10 phase bins gave an excellent fit to the data ($\chi^2_\nu = 0.89$, 297 dof), showing that *Ginga* cannot distinguish between these two models for the complex low-energy absorption. The data are consistent with constant kT_{br}, ξ_{refl} and ξ_{abs} with phase, with values of $kT_{br} = 12.0^{+4.1}_{-2.7}$ keV, $\xi_{refl} = 0.0^{+190.0}_{-0.0}$ and $\xi_{abs} = 600^{+360}_{-400}$, respectively, where the errors are for 68 per cent confidence on 33 parameters of interest. These best-fitting values were then used independently in fits to the 10 phase bins, so that errors could be computed on the remaining parameters. The results are shown in Table 7, with the incident and reflected spectra plus residuals for phase bin 7 plotted in Fig. 2(d).

As the results show, the ionized absorbing column density varies with phase, reaching a maximum of $1.8 \pm 0.2 \times 10^{23}$ cm^{-2} at phase $\phi = 0.75$. This smooth variation of column with phase seems, at first sight, to be more likely than the constant column derived from the partial-covering fits, but see the more detailed discussion in Section 4 below. The edge from this absorber is deeper than that obtained from the partial-covering model, and is at a higher energy. Thus the residual edge that is fitted by the reflection spectrum is smaller and at lower energies, and so the ionization state of the reflected spectrum is reduced. The remaining parameters are quite similar to those obtained from the partially covered reflection fits, except that the variation of N_{refl}/N_{br} with phase is no longer as smooth.

4 DISCUSSION

As described above, the model fits to the phase-resolved spectra that do not include reflection require a bremsstrahlung temperature of $kT_{br} = 19$ keV, along with a 6.7-keV iron line of large equivalent width ($\approx$600–700 eV depending on the model), when the source intensity is at its maximum at phase $\phi = 0.65$. This line energy and equivalent width are both inconsistent with those expected for thermal line emission from a plasma of solar abundances at this temperature (Makashima 1986).

The inclusion of reflection hardens the spectra above 10 keV, allowing a lower temperature continuum to be fitted, which thus increases the amount of thermal line emission. This, together with fluorescence from the white dwarf surface, provides a way of producing the observed amount of

Table 7. Summary of the parameters obtained for the reflection fits with an ionized absorber to all phase bins. kT_{br}, ξ_{refl} and ξ_{abs} were fixed at 12.0 keV, 0 and 606, respectively (see text). Errors are 68 per cent, $\Delta\chi^2 = 4.72$, confidence estimates.

Phase bin (phase range)	N_{br}[a] ($\times 10^{-3}$)	N_{refl}[b] ($\times 10^{-3}$)	N_{refl}/N_{br}	$W^c_{6.4}$ (keV)	N_H (10^{22} cm^{-2})	χ^2_ν (30 d.o.f.)
1 (0.0–0.1)	$1.17^{+0.04}_{-0.03}$	< 0.3	0.12 ± 0.12	$0.05^{+0.11}_{-0.05}$	< 0.73	1.04
2 (0.1–0.2)	$0.72^{+0.04}_{-0.04}$	< 0.6	0.38 ± 0.38	$0.03^{+0.21}_{-0.03}$	< 1.15	1.50
3 (0.2–0.3)	$2.36^{+0.17}_{-0.10}$	< 2.6	0.54 ± 0.54	$0.06^{+0.08}_{-0.06}$	< 1.89	0.72
4 (0.3–0.4)	$5.28^{+0.19}_{-0.19}$	$10.8^{+1.6}_{-1.6}$	2.05 ± 0.31	$0.05^{+0.04}_{-0.04}$	$6.2^{+1.2}_{-1.1}$	1.18
5 (0.4–0.5)	$6.83^{+0.20}_{-0.20}$	$15.4^{+1.6}_{-1.6}$	2.26 ± 0.24	$0.14^{+0.04}_{-0.04}$	$9.1^{+0.8}_{-0.9}$	0.72
6 (0.5–0.6)	$7.84^{+0.31}_{-0.35}$	$20.4^{+2.4}_{-2.2}$	2.62 ± 0.31	$0.16^{+0.04}_{-0.04}$	$14.2^{+1.6}_{-1.9}$	0.71
7 (0.6–0.7)	$8.21^{+0.35}_{-0.39}$	$18.5^{+2.8}_{-2.6}$	2.27 ± 0.35	$0.14^{+0.05}_{-0.04}$	$16.6^{+1.6}_{-1.9}$	0.52
8 (0.7–0.8)	$8.47^{+0.31}_{-0.34}$	$15.6^{+2.5}_{-2.3}$	1.86 ± 0.29	$0.12^{+0.04}_{-0.04}$	$18.2^{+1.4}_{-1.6}$	0.73
9 (0.8–0.9)	$6.57^{+0.27}_{-0.31}$	$14.7^{+2.1}_{-1.9}$	2.26 ± 0.32	$0.09^{+0.04}_{-0.04}$	$13.0^{+1.7}_{-2.1}$	0.99
10 (0.9–1.0)	$4.23^{+0.16}_{-0.16}$	$7.0^{+1.4}_{-1.5}$	1.66 ± 0.35	$0.01^{+0.04}_{-0.01}$	$7.5^{+1.1}_{-1.2}$	0.63

[a]Bremsstrahlung normalization; [b]reflected normalization; [c]6.4-keV line equivalent width.

line emission, and fits the data well. Fig. 3 shows the variation of the parameters obtained from the reflection fits with partial covering presented in Table 6, and Fig. 4 shows those derived from the ionized absorber. Only the best-fitting values of the amount of reflection and its ionization state change in response to the different description of the complex low-energy absorption. We now discuss the phase-resolved fitted parameters shown in Figs 3 and 4.

4.1 The nature of the low-energy absorption

For the values of inclination and magnetic colatitude of the main accreting pole in AM Her, the accretion stream does not cross the line of sight to the X-ray-emitting region as is the case for other polars (e.g. EF Eri; Watson et al. 1989), and we do not see an absorption dip (King & Williams 1985). The source is, however, extended over the polar cap, and so the section of the emission region that is closest to the observer will have a much smaller path length through the absorbing column than those on the far side. This differential absorption may well be mimicked by a partial-covering model if the material is neutral. Some phase variation is expected, because when the magnetic polecap is viewed near to face-on, we look through larger amounts of accreting material surrounding the hard X-ray emission region. This implies, however, that both N_H and C_F would change smoothly with phase as the accreting column rotates into view. This clearly does not happen.

This picture is probably an extreme simplification of the properties of the accretion column. The requirement of 'blobby' accretion to explain the soft X-ray excess seen in this object (Frank, King & Lasota 1988) implies that the intrinsic absorption is inhomogeneous, with denser material embedded in the accretion column. This denser material is likely to be neutral, but the rest of the accretion column is expected to be ionized (Imamura & Durisen 1983). Thus the true situation is likely to be differential covering by an ionized absorber due to the extended nature of the source and column, together with partial covering by the cold material of the dense blobs. The modelling of such a column is beyond the scope of this paper, as it requires higher-resolution data to separate out the contribution of the cold and ionized material.

4.2 N_{br} – the bremsstrahlung normalization

The bremsstrahlung normalization is clearly modulated with the source intensity, reaching a maximum when the source is face-on at $\phi = 0.65$. As this parameter is proportional to the (volume) emission measure, it suggests that the amount of emitting material presented to the observer is also varying (with a ratio of approximately 7:1 between $\phi = 0.65$ and $\phi = 0.15$). The simplest way to produce this effect is to have an extended emission region near the white dwarf surface, orientated so that a fraction is occulted as it passes over the limb (the published values of the inclination and colatitude for AM Her are such that the angle between the line of sight and the X-ray-emitting region approaches 90° when it is on the limb). Indeed, high-quality polarization data on AM Her (Wickramasinghe et al. 1991) can be explained by assuming a ~10° linearly extended (mainly in magnetic latitude) cyclotron component from the main (i.e. hard X-ray) pole, in addition to a similar component from the second pole. Alternatively, if the emitting region is in a trench, caused by the ram pressure of the accretion stream depressing the atmosphere by a few scaleheights (e.g. Beuermann 1989), a similar variation may occur.

4.3 N_{refl} – the reflection normalization

The normalization of the reflected component is also modulated with phase. This is expected, as the viewing angle between the observer and the white dwarf surface below the emission region changes throughout the orbit. When the emission region is on the limb of the white dwarf ($\phi \sim 0.15$), the reflected photons have to travel along a larger path-length through the material before escaping, and can be more easily absorbed than when the system is viewed face-on. Thus reflection is suppressed at large viewing angles.

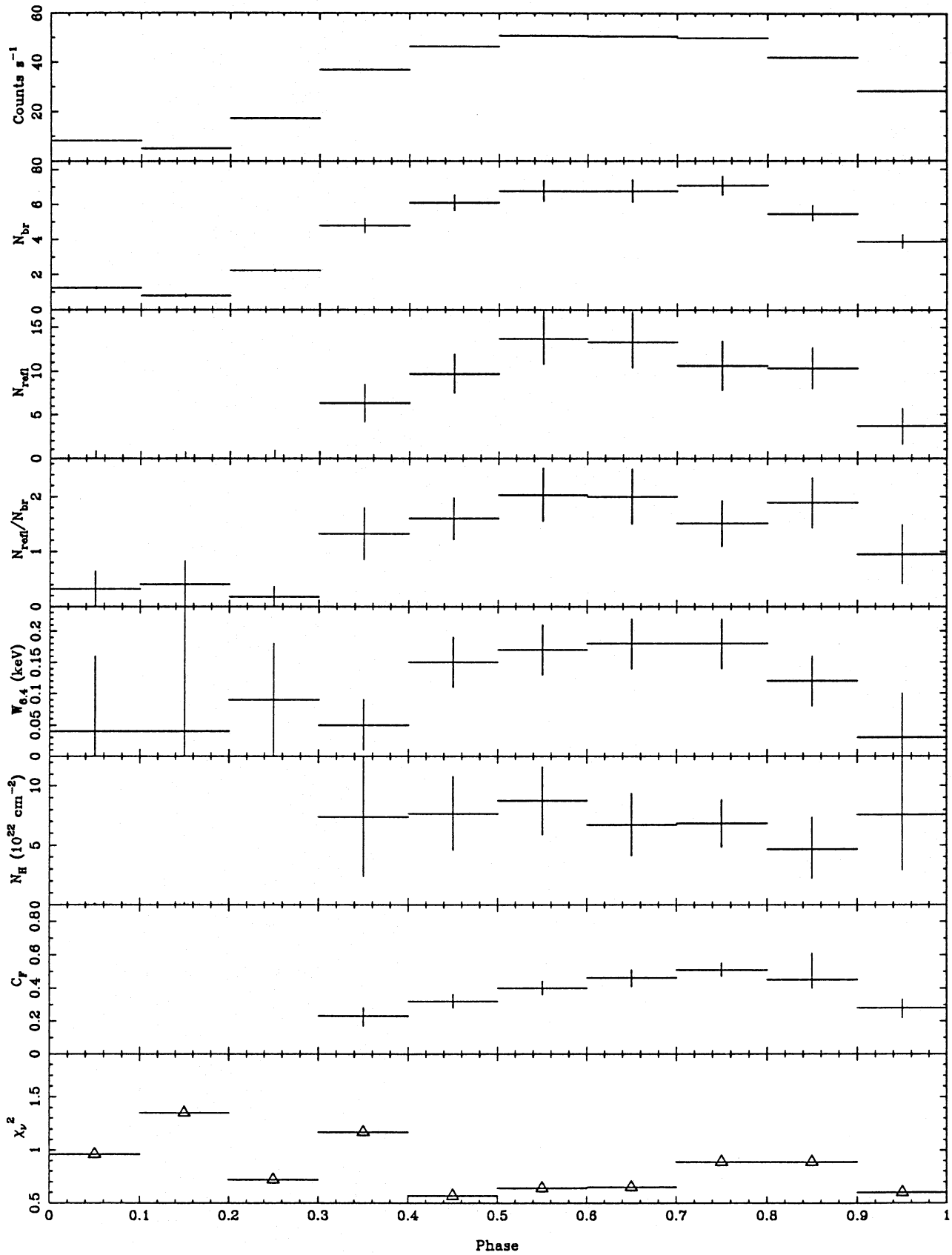

Figure 3. Variation of the parameters obtained from the partially covered reflection fits with source intensity for a 13.5-keV input spectrum and $\xi_{refl} = 140$. From the top panel down: 2–18 keV light curve; bremsstrahlung normalization; reflection normalization; relative normalization; fluorescent 6.4-keV line equivalent width (keV); absorbing column density (10^{22} cm^{-2}); covered fraction; reduced χ^2.

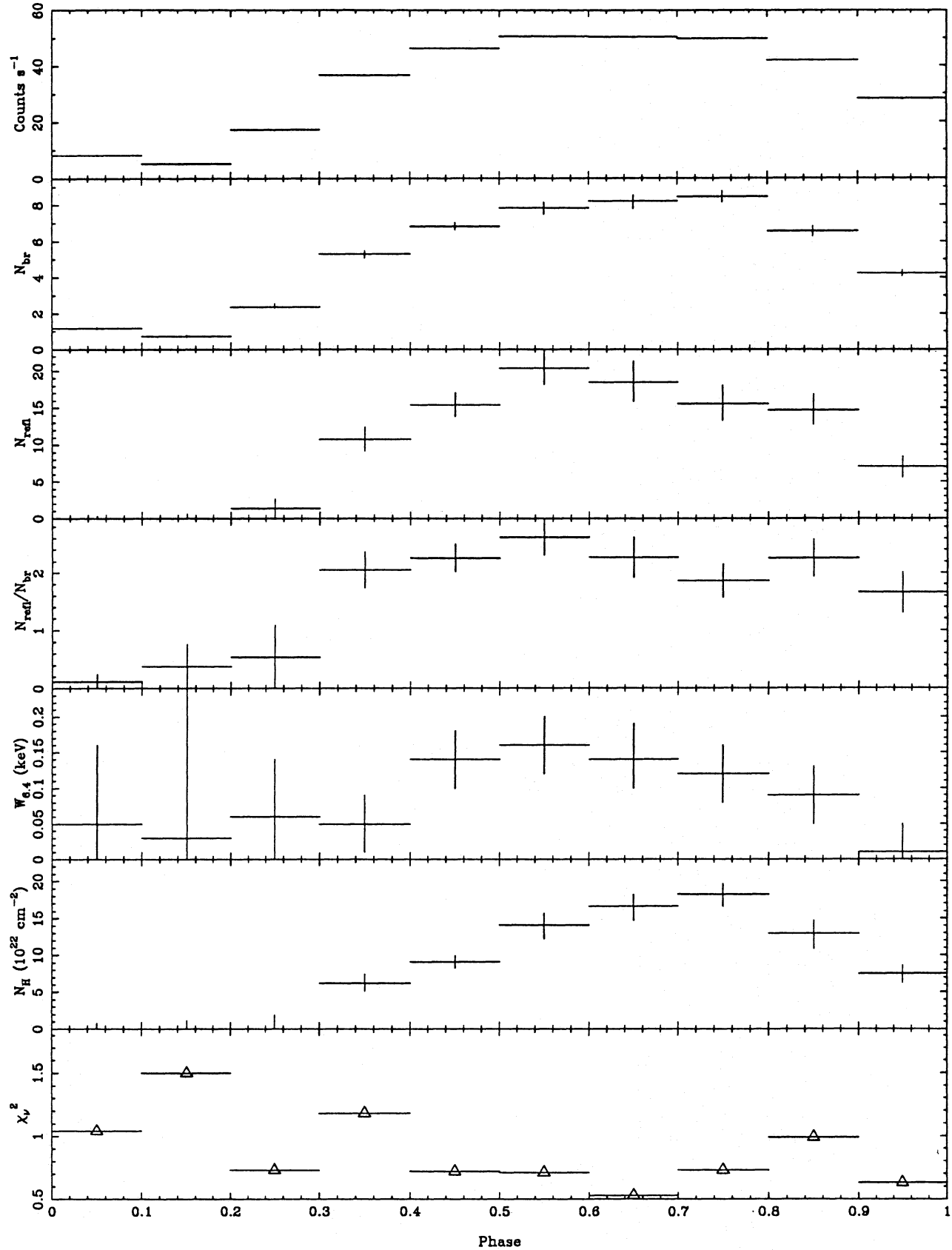

Figure 4. Variation of the parameters obtained from the ionized absorber reflection fits with source intensity for a 12.0-keV input spectrum, $\xi_{\rm refl}=0$, and $\xi_{\rm abs}=606$. From the top panel down: 2–18 keV light curve; bremsstrahlung normalization; reflection normalization; relative normalization; fluorescent 6.4-keV line equivalent width (keV); ionized absorbing column density (10^{22} cm^{-2}); reduced χ^2.

4.4 $N_{\rm refl}/N_{\rm br}$ – the relative normalization

The ratio of the two normalizations is proportional to the projected solid angle (Ω) of the reprocessing material, with respect to the shock front. Again, this is modulated, as the amount of reflection increases as we approach the perpendicular to the white dwarf surface below the emitting region. At the minimum viewing angle ($\phi = 0.65$), we observe $N_{\rm refl}/N_{\rm br} = 2.0 \pm 0.5$ for the partial-covering fits, and $N_{\rm refl}/N_{\rm br} = 2.4 \pm 0.4$ for the ionized absorber. The ratio $N_{\rm refl}/N_{\rm br}$ for material subtending a solid angle of $\Omega/2\pi$ to the illuminating X-ray source, and where the reflection spectrum is calculated by the angle-averaged approximation of Lightman & White (1988), is given by Ghisellini, Haardt & Matt (1994) as

$$f(\mu) = \frac{3\mu}{4}\left[(3 - 2\mu^2 + 3\mu^4)\log\left(1 + \frac{1}{\mu}\right) + (3\mu^2 - 1)(0.5 - \mu)\right], \quad (1)$$

where $\mu = \cos(\theta)$, where θ is the viewing angle between the normal to the reflecting surface and the line of sight. At the hard flux maximum, where the emission region is closest to face-on, this predicts $N_{\rm refl}/N_{\rm br} \sim 1.3$, slightly lower than that derived from the spectral fits but consistent with the white dwarf surface subtending a solid angle of 2π, as there is a $\sim$ 10 per cent difference in the reflection normalization for slightly hotter reprocessing material ($T \approx 5 \times 10^5$ K).

A more detailed check can be made by calculating the viewing angle at each phase from the magnetic colatitude and inclination of the system (Cropper 1990), and fitting the theoretical functional form of the reflected normalization as a function of phase shown above. This gives $1.0 \leq \Omega/2\pi \leq 1.5$ (a best fit of 1.3 gives $\chi^2 = 8.0$ for 9 dof) for the partial-covering fits and $1.5 \leq \Omega/2\pi \leq 1.8$ (a best fit of 1.67 gives $\chi^2 = 38$ for 9 dof) for the ionized absorber. The large solid angle implied for the reflected normalization from the ionized absorber description of the low-energy X-ray leakage can be produced if the white dwarf surface is depressed at the base of the hard X-ray-emitting column. Alternatively, the same apparent effect is obtained if the reflecting material on the white dwarf surface has abundances less than solar (George & Fabian 1991). This is because a reduced heavy-element abundance reduces the opacity of the reflecting material, which in turn increases the probability of reflection. The unacceptable fit to the predicted phase-dependence of the reflection normalization favours the former interpretation, as the reflecting surface is then not flat, and so predicts a different phase-dependence from that given by equation (1).

On the other hand, the partially covered reflection model is consistent with the phase-dependence and amount of reflection predicted from solar abundance material subtending a solid angle of $\sim 2\pi$, as is expected for the reflection of X-ray photons from the white dwarf surface that were originally produced near a shock front whose height $h \ll R_{\rm wd}$ (where $R_{\rm wd}$ is the white dwarf radius).

4.5 $W_{6.4}$ – the fluorescent 6.4-keV line equivalent width

The fluorescent 6.4-keV iron line emission is expected to be roughly proportional to the amount of reflecting material on view to the observer, and therefore should correlate with $N_{\rm refl}$. At maximum, we observe $W_{6.4} = 180 \pm 40$ eV for the partial-covering fits and $W_{6.4} = 140 \pm 40$ eV for the ionized absorber fits. Basko (1978) shows a method for calculating the expected fluorescent line equivalent width, accurate to 5 per cent. We can renormalize the fluorescent equivalent width obtained from one incident X-ray spectrum to another, using

$$W(\theta) \propto \int_{E_{\rm th}}^{\infty} \frac{L(E)\,{\rm d}E}{L(E_{\rm K})\,E^3}, \quad (2)$$

where $L(E)$ is the spectrum of the source at energy E, θ is the angle between the line of sight and the normal to the reflecting material, $E_{\rm th} = 7.11$ keV is the threshold energy for K-shell absorption, and $E_{\rm K} = 6.4$ keV is the fluorescent line energy. Using the Monte Carlo calculations of George & Fabian (1991) [$W_{6.4}(0) = 160$ eV for a power-law incident spectrum of energy index 0.7], we obtain $W_{6.4}(0) \approx 120$–150 eV for an input thermal bremsstrahlung spectrum with $kT_{\rm br} = 10$–17 keV. Our observed 6.4-keV fluorescent line equivalent width appears to be consistent with that expected for the observed amount of reflection.

A more detailed check can again be made by fitting the expected functional form of the variation in line equivalent width with respect to the inclination of the emission region, given by Ghisellini, Haardt & Matt (1994) as

$$W(\mu) = \frac{W(0)}{\ln 2}\,\mu \ln\left(1 + \frac{1}{\mu}\right). \quad (3)$$

The ionized absorber model gave a good fit with a face-on equivalent width of $97 < W_{6.4} < 160$ eV, with a mean of 128 eV. This is, however, inconsistent with the reflection normalization obtained for this model, which predicts substantially more cold line emission. The partially covered reflection model also gave a good fit, with a face-on equivalent width of $140 < W_{6.4} < 200$ eV ($\chi^2 = 4$ for 9 dof), although it was slightly higher than the 130 eV expected from a 13.5-keV plasma if the surface has solar abundances and subtends a solid angle of $\Omega/2\pi = 1$. This suggests that $\Omega/2\pi \sim 1.3$, which can be produced if the white surface is depressed at the base of the hard X-ray-emitting accretion column, providing a larger solid angle of reprocessing material. Alternatively, we would get the same apparent effect if the reflecting material on the white dwarf surface had abundances ~ 30 per cent less than solar (George & Fabian 1991). This is because a reduced heavy-element abundance will lower the opacity of the reflecting material, which in turn increases the probability of the fluorescent photons escaping.

4.6 Density of the reflecting material

The ionization parameter $\xi = L/N_{\rm e}R^2$ can give us information about either the electron density of the reflecting medium or the shock height of the thermal emitting region. An expression for the shock height has been given by Beuermann (1989):

$$h({\rm cm}) = 9 \times 10^5 B_7^{-1} n_{14}^{1/2} R_9^{-4}, \quad (4)$$

where B_7 is the magnetic flux density (in units of 10^7 gauss), n_{14} is the electron number density at the magnetic capture

radius (10^{14} cm^{-3}), and R_9 is the white dwarf radius (10^9 cm). For AM Her, $B_7 = 1.3$, $n_{14} = 0.1$–2.0 and $R_9 = 0.7$ (from Cropper 1990 and Liebert & Stockman 1985), and we find $h = 0.003$–$0.013 R_{wd}$. This compares well with that estimated by Rothschild et al. (1981), $h = 0.01 R_{wd}$, from the eclipse length of the hard X-ray light curve. Therefore, using the best-fitting value of $\xi = 140$–0 (where the range in ξ is from the partial-covering and ionized absorber fits, respectively), we find $N_e \gtrsim 10^{17}$ cm^{-3} for the reflecting medium. At these high densities, however, three-body recombination, which is neglected in the ionization calculations, will be important. The effect of this would be to raise the recombination rate, thereby lowering the value of N_e, assuming ξ/α (in appendix B of Done et al. 1992) remains constant.

We can compare this with the white dwarf surface density. By using the hydrostatic equilibrium condition, it can also be shown that the number density at the white dwarf photosphere ($\tau = 1$) is $N_{wd} \sim 10^{24}/T(\mathrm{K}) \sim 5 \times 10^{18}$ cm^{-3} (where $T \approx 2 \times 10^5$ K is the white dwarf photospheric temperature). Given the approximations in the reflection calculations, the agreement between N_e and N_{wd} is quite good, especially as there is a large error range on ξ.

4.7 Temperature

The inclusion of the reflected component allows the underlying thermal continuum temperature to be constant at $kT_{br} \approx 13.5$ keV (for the partial-covering model) for all phase bins. Whereas in the non-reflection fits an increase in kT_{br} of a few keV was required between phases $\phi \approx 0.15$ and 0.65, with a value of 21 keV at $\phi \approx 0.65$ that was too high to account for the observed iron line energy and equivalent width. This apparent effect can be explained by reflection as the spectrum is hardened towards face-on at $\phi \approx 0.65$ by the albedo of the white dwarf. The lower temperature continuum required by the fits including reflection suggests that the implied bremsstrahlung luminosity will be reduced in comparison to that implied by the non-reflection fits. For example, at $\phi \approx 0.65$ the ratio of the total bremsstrahlung luminosity without reflection ($L_{br} \approx 3.68 \times 10^{-10}$ erg cm^{-2} s^{-1}) to that from a fit including reflection ($L_{br} \approx 2.27 \times 10^{-10}$ erg cm^{-2} s^{-1}) is 1.6. This suggests that the 'soft X-ray problem' (in which the luminosity of the soft X-ray component is greater than that of the illuminating hard X-ray component from which it was thought to derive) may be worse than has commonly been realized.

The simple strong shock models predict $kT_s = 31.9 M_1 R_9^{-1}$ (e.g. Frank, King & Raine 1992), where M_1 is the white dwarf mass (in solar masses) and R_9 is the white dwarf radius (in 10^9 cm). For AM Her, $M_1 \sim 0.75$ (Mukai & Charles 1987) and $R_9 \sim 0.77$, giving $kT_s \sim 31$ keV. The shocked gas is expected to settle on to the white dwarf, cooling as it does so. This suggests that a continuous range of temperatures below kT_s might be seen, with a significant contribution from lower temperatures. Our data are, however, adequately described by a single temperature. The existence of a substantial quantity of low-temperature plasma (e.g. 2–5 keV) can be ruled out on the basis of the observed line equivalent width, which would be much larger for lower temperature emission. The single temperature we observe probably represents an average over the emission region.

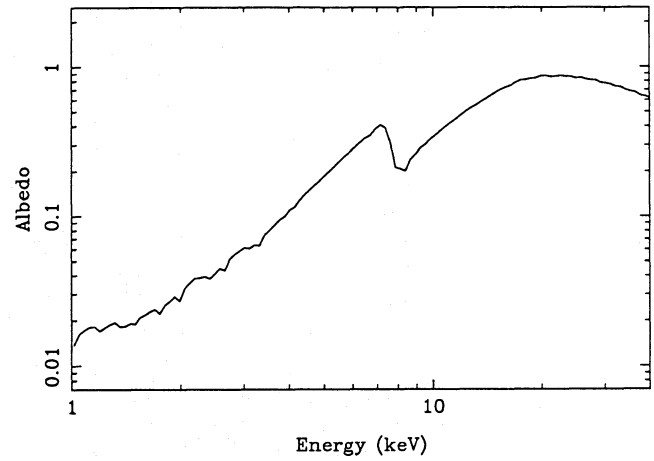

Figure 5. The X-ray albedo as a function of energy at phase $\phi = 0.65$.

4.8 X-ray albedo

An important consequence of the reflection model is that a direct measurement of the X-ray albedo (A_x) can be made. Fig. 5 shows the albedo, calculated as the ratio of the reflected continuum to incident continuum for the face-on data at phase $\phi \approx 0.65$ for the partial-covering model. The albedo is clearly energy-dependent. Starting with $A_x \approx 0.02$ at 1–2 keV, the albedo then increases almost linearly with energy (in logarithmic space) with a slope ~ 1.45, reaching a maximum of $A_x \approx 0.8$ at 20 keV, and decreasing beyond. The average albedo over 1–40 keV is $A_x \approx 0.35$, similar to that obtained by Felsteiner & Opher (1976). As most of the hard X-ray flux occurs in the 2–30 keV band, the assumption of $A_x = 0.3$ in soft X-ray excess calculations (e.g. King & Watson 1987) is a good one.

4.9 The hardness ratio variation

In light of the above results, how do we explain the hardness ratio variation depicted in Fig. 1(b)? It appears there are two processes responsible. Below ~ 7 keV, the complex absorption column is the main cause of the variation, with more absorption at phases corresponding to the X-ray maximum (this is seen as an increase in the covered fraction and column in the partial-covering and ionized absorber models, respectively). Above ~ 7 keV, the X-ray albedo becomes dominant, allowing greater reflection of harder X-rays when the X-ray-emitting region is seen closest to face-on. Indeed, a hardness variation is also observed for the ratio of 9.9–18.0 keV to 7.5–9.9 keV fluxes.

4.10 The iron absorption edge

The fits in Section 3.4 showed that the high-energy data could be phenomenologically described by a model with a bremsstrahlung continuum, an iron line and an edge. Only an edge from highly ionized iron gave a significant improvement over previous models, which is seemingly in contradiction to the rather moderate ionization states derived for the reflector and absorber in the partial-covering and ionized absorber fits, respectively. This is again due to the fact that, without

the inclusion of reflection, the continuum temperature is artificially high. This distorts the spectral shape, so that the recovered edge energy is not necessarily indicative of the ionization state of the material.

4.11 Comparison with other results

The previous bremsstrahlung temperature determination for AM Her made from *HEAO-1* hard X-ray data by Rothschild et al. (1981) was found to be 30.9 ± 4.5 keV for data fitted above ~ 10 keV. By similarly fitting the *Ginga* data from phase $\phi = 0.65$ with a simple thermal model, a temperature of 21^{+10}_{-6} keV is obtained, consistent with Rothschild et al. (1981). As AM Her was at a similar X-ray intensity for both the *Ginga* and *HEAO-1* data, this suggests that, when no allowance for reflection is made, the continuum temperatures in polars will be overestimated.

Even the approximation of the effects of reflection by including a heavily absorbed bremsstrahlung component did not reduce the temperature of the *HEAO-1* fits significantly. This is because the spectrum obtained from reflection is much broader than that obtained from absorption, with much more emission at lower energies from photons reflected at small optical depths in the material. With an absorbed spectrum, all the low-energy photons are required to travel though the large column, and so the spectrum cuts off rapidly at low energies. This difference in the two spectral shapes means that absorption does not provide a good approximation to the reflected spectrum; it is much more peaked, and so cannot contribute enough at low energies to allow the intrinsic spectrum to steepen.

Van Teeseling, Heise & Paerels (1993) have recently analysed the soft X-ray spectrum from the *EXOSAT* LE grating observations of AM Her first described by Heise et al. (1985). During that observation, AM Her was in the reversed mode, where the soft X-ray light curve was shifted by $\sim 180°$ with respect to the linear polarization ephemeris, whereas the hard X-ray light curve was not. This was interpreted as evidence for two-pole accretion. These authors modelled the soft X-ray emission as that caused by the deposition of energy (by irradiation or blobs) at the white dwarf surface. Their data favour models in which the white dwarf surface temperature gradient is much flatter than that expected if all the energy is deposited at large optical depths, as in the original blob accretion models (Frank, King & Lasota 1988). Their best model fit is found when the soft X-rays are produced from irradiation of the white dwarf surface by a hard X-ray component. Thus in that observation, if soft X-rays are from reprocessed hard X-rays, then the associated hard X-ray source must be heavily obscured, as the hard X-ray light curve has a minimum at the phase of the soft X-ray maximum. As this hard X-ray emission illuminates the white dwarf surface, however, it must produce a strong reflection component from the new soft X-ray pole, visible at phase 0.15. While the lack of soft X-ray data means that we cannot tell whether our observation was in the normal or reversed mode, if the system was in the latter mode (and, indeed, the *Ginga* hard X-ray light curve and hardness ratio are very similar to those seen with *EXOSAT* during the reversed mode) then we can rule out illumination as the origin of the soft X-ray flux, as we see a minimum in reflection at this phase. We see that the reflection component has a maximum at phase 0.65 in the *Ginga* data, suggesting the hard X-ray emission arises solely from near the main pole. This, coupled with the soft X-ray luminosity excess, favours instead the alternative suggestion of van Teeseling, Heise & Paerels (1993) of a blob accretion model, where the energy is deposited at optical depths of $\tau \sim 1$. Dense inhomogeneities in the accretion flow penetrate further in azimuth around the magnetosphere of the white dwarf until they attach to field lines emanating from near the second pole, naturally producing soft X-rays from a region that is $\sim 180°$ out of phase with the hard X-ray light curve (see Wickramasinghe et al. 1991 for a similar argument based on optical data).

5 CONCLUSIONS

The results obtained above are summarized as follows. The observed phase-resolved *Ginga* hard X-ray spectrum of AM Her is best described by allowing for reflection of X-rays from material subtending a solid angle of $\sim 2\pi$ with respect to the thermal emitting region, consistent with the white dwarf surface. By introducing such a reflected component, the thermal continuum temperature required to fit the spectra can be reduced. This allows more thermal iron line emission, and, together with iron-Kα fluorescence obtained from reflection, correctly provides the observed amount of line emission, which could not be explained otherwise.

The results above clearly predict that both a 6.4-keV fluorescent line and a thermal line blend at 6.8 keV should be observed in future X-ray observations of AM Her made with instrumentation of greater energy resolution in the 2–10 keV range (e.g. ASCA and JET-X). Also, together with *ROSAT* data, we should be able to determine the relative importance of the cold and ionized absorption.

ACKNOWLEDGMENTS

CD acknowledges a SERC fellowship. Part of this work was completed when APB was in receipt of a SERC studentship.

REFERENCES

Bai T., 1979, Sol. Phys., 62, 113
Basko M. M., 1978, ApJ, 223, 268
Beuermann K., 1989, in Coyne S. J. G. V., Moffat A. F. J., Tapia S., Magalhaes A. M., Schulte-Ladbeck R., Wickramasinghe D. T., eds, Polarized Radiation of Circumstellar Origin. Vatican Observatory, Vatican City, p. 125
Cropper M., 1990, Space Sci. Rev., 54, 195
Crosa L., Szkody P., Stokes G., Swank J., Wallerstein G., 1981, ApJ, 247, 984
Done C., Mulchaey J. S., Mushotzky R. F., Arnaud K. A., 1992, ApJ, 395, 275
Felsteiner J., Opher R., 1976, A&A, 46, 189
Frank J., King A. R., Lasota J. P., 1988, A&A, 193, 113
Frank J., King A. R., Raine D. J., 1992, Accretion Power in Astrophysics, second edn. Cambridge Univ. Press, Cambridge
George I. M., Fabian A. C., 1991, MNRAS, 249, 352
Ghisellini G., Haardt F., Matt G., 1994, MNRAS, 267, 743
Hayashida K. et al., 1989, PASJ, 41, 373
Heise J., Brinkman A. C., Gronenschild E., Watson M., King A. R., Stella L., Kieboom K., 1985, A&A, 148, L14
Imamura J. N., Durisen R. H., 1983, ApJ, 268, 291
Ishida M., 1991, PhD thesis, Univ. Tokyo

Ishida M., Makishima K., Mukai K., Masai K., 1994, MNRAS, 266, 367
Kallman T. R. et al., 1993, ApJ, 411, 869
King A. R., Watson M., 1987, MNRAS, 227, 205
King A. R., Williams G. A., 1985, MNRAS, 215, 1P
Liebert J., Stockman H. S., 1985, in Lamb D. Q., Patterson J., eds, Cataclysmic Variables and Low-mass X-ray Binaries. Reidel, Dordrecht, p. 151
Lightman A. P., White T. R., 1988, ApJ, 335, 57
Makishima K., 1986, in Mason K. O., Watson M. G., White N. E., eds, The Physics of Accretion onto Compact Objects. Springer-Verlag, Berlin, p. 249
Matt G., Perola G. C., Piro L., 1991, A&A, 247, 27
Morrison R., McCammon D., 1983, ApJ, 270, 119
Mukai K., Charles P. A., 1987, MNRAS, 226, 209
Norton A. J., Watson M. G., 1989, MNRAS, 237, 853
Norton A. J., Watson M. G., King A. R., 1991, in Treves A., Perola G. C., Stella L., eds, Iron Line Diagnostics in X-ray Sources. Springer-Verlag, Berlin, p. 155
Pounds K. A., Nandra K., Stewart G. C., George I. M., Fabian A. C., 1990, Nat, 344, 132
Raymond J. C., Smith B. W., 1977, ApJS, 35, 419
Rothschild R. E. et al., 1981, ApJ, 250, 723
Shafer R. A., Haberl F., Arnaud K. A., Tennant A. F., 1991, XSPEC User Guide. ESA, Paris
Singh J., Swank J., 1993, MNRAS, 262, 1000
Swank J. H., Fabian A. C., Ross R. R., 1984, ApJ, 280, 734
Tuohy I. R., Mason K. O., Garmire G. P., Lamb F. K., 1981, ApJ, 245, 183
Turner M. J. L. et al., 1989, PASJ, 41, 345
van Teeseling A., Heise J., Paerels F., 1993, A&A, 281, 119
Watson M. G., King A. R., Jones M. H., Motch C., 1989, MNRAS, 237, 299
Wickramasinghe D. T., Bailey J., Meggitt S. M. A., Ferrario L., Hough J., Tuohy I. R., 1991, MNRAS, 251, 28
Yaqoob T., 1991, PhD thesis, Univ. Leicester
Yoshida K., Mitsuda K., Ebisawa K., Ueda Y., Fujimoto R., Yaqoob T., Done C., 1993, PASJ, 45, 605